

# F30: CCD photometry in modern astronomy

carried out by

**Mathieu Kaltschmidt and Quirinus Schwarzenböck**

on August 27<sup>th</sup> / 28<sup>th</sup> 2018

at

**Max-Planck-Institut für Astronomie**

Königstuhl 17  
69117 Heidelberg

**Supervisor:** Asmita Bhandare

handed in as special report on: *November 21, 2018*

Graded: \_\_\_\_\_

Date, Signature



---

## F30: CCD photometry in modern astronomy

Mathieu Kaltschmidt and Quirinus Schwarzenböck

### Abstract

This experiment has been performed as part of the advanced lab course for physics students (FP) at Heidelberg University.

The theoretical and experimental basics needed for the understanding of the conducted measurements is introduced and important concepts of modern astronomical research are presented and discussed.

The characteristics of a CCD are analyzed using data we recorded with the KING telescope at MPIA.

Furthermore important astronomical data analysis tools used in current research are applied to our measurements.

Lastly we use an image of the globular cluster BS90<sup>14</sup> taken by the Hubble Space Telescope (HST) to generate a Color-Magnitude diagram in order to determine age and metallicity of the cluster.

### Zusammenfassung

Dieses Experiment wurde im Rahmen des Fortgeschrittenen-Praktikums für Studierende der Physik (FP) an der Universität Heidelberg durchgeführt.

Es werden die theoretischen und experimentellen Grundlagen zum Verständnis der durchgeführten Messungen vorgestellt und grundlegende Konzepte moderner astronomischer Forschung erläutert und diskutiert.

Die charakteristischen Eigenschaften einer CCD werden am Beispiel unserer Messungen mit dem KING Teleskop am MPIA überprüft und wichtige Elemente der astronomischen Datenanalyse angewendet.

Am Beispiel einer Aufnahme des Kugelsternhaufens BS90<sup>14</sup>, welche vom Hubble Space Telescope (HST) aufgezeichnet wurde, wird ein Farben-Helligkeits-Diagramm erstellt und damit das Alter und die Metallizität des Sternhaufens ermittelt.



# Contents

<b>1 Fundamental principles of astronomical measurements</b>	<b>1</b>
1.1 Detectors in Astronomy . . . . .	1
1.2 Data Reduction . . . . .	2
1.3 Basics of photometry . . . . .	3
1.4 Magnitudes . . . . .	4
1.4.1 Instrumental Magnitude . . . . .	4
1.4.2 Apparent Magnitude . . . . .	4
1.4.3 Absolute Magnitude . . . . .	4
1.5 Bolometric Magnitude . . . . .	5
1.6 The Hertzsprung-Russel Diagram . . . . .	6
1.7 Stellar clusters . . . . .	8
1.7.1 Open clusters . . . . .	8
1.7.2 Globular clusters . . . . .	9
<b>2 Layout of the experiment</b>	<b>10</b>
<b>3 Characteristics of the experimental setup</b>	<b>11</b>
3.1 The cooling process . . . . .	11
3.2 Flat field corrections . . . . .	13
3.3 Linearity and dynamical range of the CCD . . . . .	15
3.4 Sensitivity of the detector and noise properties . . . . .	16
<b>4 Globular Cluster BS90<sup>14</sup></b>	<b>19</b>
4.1 Zeropoint calibration . . . . .	19
4.2 PSF photometry with STARFINDER . . . . .	20
4.3 Color Magnitude Diagram for BS90 <sup>14</sup> . . . . .	22
<b>5 Discussion of our results</b>	<b>24</b>
<b>List of Figures</b>	<b>I</b>
<b>References</b>	<b>II</b>



# 1 Fundamental principles of astronomical measurements

Most times we are trying to obtain astronomical data by measuring electromagnetic radiation. Unfortunately there are two basic problems with this approach. On the one hand we are dealing with huge distances in space, which lead to very small intensities and on the other hand we can not achieve any kind of laboratory conditions like in space, due to the mere lack of a laboratory big enough.

## 1.1 Detectors in Astronomy

The evolution of detectors in astronomy started simple, with people looking in the sky. Soon astronomers realized that it is more precise and reliable to take pictures. But even analogue pictures did not allow accessibility and useful comparison of the measured data, so ultimately scientists were lead to the development of today's standard, charged couple devices (CCDs).

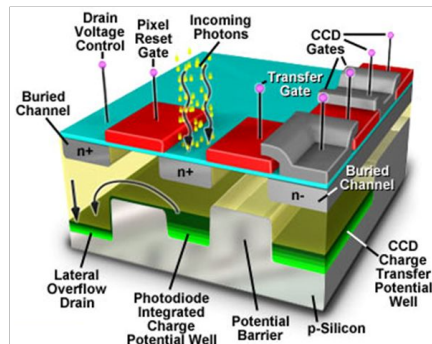
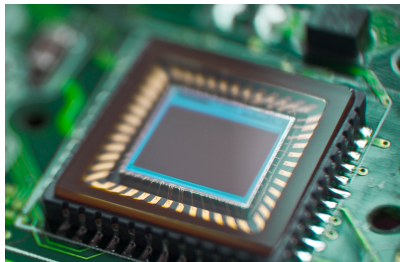


**Figure 1.1:** Image of a CCD chip<sup>1</sup> and a schematic overview of its functionality<sup>2</sup>.

These are semiconductor detectors, that use the inner photoelectric effect to convert incoming radiation into a separated charge that can be read out. A CCD consists of a two dimensional grid of light sensitive metal oxide semiconductors, that act as capacitors. Incoming photons excite electrons into the conduction band, after which the electrons are trapped in the capacitors potential wells. At this point, they can easily be read out and

<sup>1</sup>Photo by Matt Laskowski: <https://www.flickr.com/photos/fox-orian/1234526868> (16.11.18)

<sup>2</sup>Taken from: <http://hamamatsu.magnet.fsu.edu/articles/ccdanatomy.html> (16.11.18)

converted into a digital signal.

This technique had such a big impact on astronomy because of the following fundamental advantages compared to other light detectors:

**High sensitivity:** CCDs achieve a quantum efficiency of up to 90 %, meaning the chips are able to capture almost all of the incoming photons.

**High dynamic range:** The dynamic range characterises the devices ability to distinguish different brightness levels. Therefore, a high dynamic range is helpful in astronomy, because we are dealing with stars that are visible with the bare eye, as well as objects we only receive single photons from.

**Linearity over almost the entire dynamic range:** The detector signal is to an amazing degree proportional to the incoming photon flux, up until the detector is saturated. This is a helpful property when comparing objects on the same, as well as on different images. Nevertheless, the exposure time should be chosen very carefully to make sure to get a useful signal to noise ratio.

**Direct availability for further computer-aided data analysis:** Unlike all analogue forms of photography and photometry the data collected by a CCD is immanently converted into a digital signal, without any quality loss or other additional problems.

Of course, as always, there are some drawbacks. For one, it has to be considered that some pixels are dead (their output has no meaning). Other pixels are activated by cosmic radiation such as  $\gamma$ -rays, muons and electrons. These pixels or even the area around them mostly appear to be saturated or have an unlikely high charge.

Both events can be counteracted by taking multiple measurements with slightly different camera angles. The dead pixels will stay at their exact position, while the pixels activated by other kinds of radiation will randomly change place. Therefore, it is possible to get rid of both errors by aligning the images and taking the median. The described technique is called *dithering* or *jittering*.

## 1.2 Data Reduction

The intensities measured over the whole area of a CCD are subject to slight variations caused by imperfections in the manufacturing process, some dirt or residue in the optical path and the general problems discussed above. To account for these points, for we want an image with comparable data, we expose a homogeneously illuminated, flat surface, either in the sky (*sky flat*) or inside the dome (*dome flat*). By dividing our measurements by the normalized *flat field* (the image we obtain as just described), we get rid of any sensitivity variations, assuming these variations are, at least over the course of the experiment, constant.

To not only be able to compare objects within our image, but with other astronomical data, we can calibrate our CCD with so called *standard stars*, i. e. stars with a well known intensity.

The last thing one has to take into account when doing measurements with a CCD is a general offset of all the pixel counts produced during the read-out process. Since this *bias* should be constant for the whole image and also unaffected by the integration time, one can easily take a short measurement with closed shutter to determine the bias of a picture. Theoretically this correction also includes the dark current produced by thermal electrons but this effect is negligible since we are working with very low temperatures, which suppress any dark current.

## 1.3 Basics of photometry

What we are observing in our measurements is the *radiation flux*  $F$  of the stars given by

$$F = \frac{L}{4\pi d^2} \quad (1.1)$$

where  $d$  is the distance between the observer and the star and  $L$  is its luminosity.

To normalize our measured values we are using the sun as reference for the units we choose. For example the luminosity of the sun is  $L_{\odot} = 3.846 \cdot 10^{26}$  W.  
The *Stefan-Boltzmann law* explains the connection between the surface temperature of a star and its flux:

$$F = \sigma T_{\text{eff}}^4 \quad (1.2)$$

with the Stefan-Boltzmann constant  $\sigma = 5.67 \cdot 10^{-8}$  Wm<sup>-2</sup>K<sup>-4</sup>. To understand the meaning of the effective temperature  $T_{\text{eff}}$  we need to know the physical definition of a black body. A black body is, in theory, an object that absorbs every radiation independent of the corresponding wavelength and doesn't reflect any of it. The effective temperature in (1.2) is the temperature a black body with the same surface area as the star would need to emit the same radiation power.

We already introduced a new quantity, the luminosity of a star which is defined as the surface area  $A$  times the flux. From this we can derive a relation between luminosity and temperature using (1.2):

$$L = 4\pi R^2 \sigma T_{\text{eff}}^4 \quad (1.3)$$

with the stars radius  $R$ .

Another interesting parameter in astronomical observations is the mass of the observed star, which determines its evolution. In particular the initial mass of the star is the parameter that allows us to predict his fate, but unfortunately the determination of star masses from single measurements is not trivial.

As one can conclude from (1.1) the intensity of the incoming flux of the star, i. e. the number of photons detected, decreases with the square of the distance. The problem is that the distance is not directly known for most observations. This and the fact that every instrumental setup is different, leads us to the introduction of different magnitude scales, to be able to determine luminosities and to compare results taken from various observations. These different scales are explained in the following section.

## 1.4 Magnitudes

To solve the problem mentioned above we introduce three different magnitude scales and another scale including the wavelength independency of the observed radiation.

### 1.4.1 Instrumental Magnitude

The instrumental magnitude allows us to compare measurements of different objects within the same measurement or during different sessions at the same instrumental setup under the same conditions.

It is a relative unit, converting the measured counts to a logarithmic scale with an arbitrary zeropoint  $p_0$ , i. e.

$$m_{\text{instr.}} = p_0 - 2.5 \log_{10}(\text{counts}) \quad (1.4)$$

With the help of so called standard stars whose magnitude is already known and the fitting of a point spread function (PSF), which will be explained in detail later on, one can transform the relative instrumental magnitude into the apparent magnitude.

### 1.4.2 Apparent Magnitude

The apparent magnitude scale takes the earth as reference point and measures the brightness of the star as perceived from its surface, assuming a logarithmic perception of the brightness by the human eye. This scale was already introduced by Hipparch at  $\sim 150$  b.c., then using brightness classes ranging from 1 (brightest stars) to 6 (barely visible). Nowadays a difference of five magnitudes corresponds to a factor of 100. With this scaling one finds the following formula for the flux ratio of two stars:

$$\frac{F_2}{F_1} = 100^{(m_1 - m_2)/5} \quad (1.5)$$

As before standard stars are used to determine the offset between instrumental and apparent magnitude and thereby calibrating the scale. Now we are able to compare different magnitudes obtained from different measurements and with different circumstances.

### 1.4.3 Absolute Magnitude

Directly resulting from the conceptual idea of the apparent magnitude we finally introduce the absolute magnitude as the apparent magnitude a star would have at a distance of 10 pc.<sup>3</sup>

The distance has been chosen arbitrarily. This allows us to physically compare the absolute brightness of different stars at different distances.

---

<sup>3</sup>The distance 1 pc = 3.263 ly =  $3.086 \cdot 10^{16}$  m.

One can calculate the ratio between the actual measured flux (the apparent magnitude  $m$ ) and the hypothetical magnitude of the flux if the star was actually 10 pc away.

$$\frac{F(10 \text{ pc})}{F} = \left( \frac{d}{10 \text{ pc}} \right)^2 = 100^{(m - M)/5} \quad (1.6)$$

In this formula,  $m$  represents the apparent magnitude and  $M$  the absolute magnitude. Now we are able to compute the absolute brightness of every star, if we know its distance  $d$  and the corresponding apparent magnitude. If the distance is, as usually, not known and other methods lead to a determination of the stars absolute brightness, we are able to use the following formula to find the distance of the observed star:

$$d = 10^{(m - M + 5)/5} \text{ [pc]} \quad (1.7)$$

where the expression  $m - M = 5 \log_{10} d[\text{pc}] - 5$  is called the distance modulus. If two stars are located at the same distance from the observer the following relation holds true:

$$\frac{F_2}{F_1} = \frac{L_2}{L_1} = 100^{(M_1 - M_2)/5} \quad (1.8)$$

As a result, for known luminosity and absolute magnitude of a reference star we can determine the luminosity of any other star at the same distance from its absolute magnitude.

## 1.5 Bolometric Magnitude

We distinguish between wavelength-dependent and bolometric magnitudes, which are integrated over the total wavelength range.

Due to limitations in the respective spectral range of the detectors it is often hard to determine the bolometric amplitude  $M_{\text{bol}}$ . We want our measurements to be as precise as possible. That's the reason why they need to be performed by space observatories, where absorption processes that occur in earth's atmosphere do not affect the measurements. If we nevertheless want to estimate the bolometric magnitude from measurements from earth, we need to introduce wavelength-dependent magnitudes  $M_\lambda$  which cover only one part of the total spectral range. To realize this we can use different well-defined filters which let us focus our measurements on specific ranges.

In the following table one of the most commonly used filter systems, the Johnson system is presented. Here  $\lambda_0$  describes the respective central wavelength and  $\delta\lambda$  the corresponding spectral width.

Filter	$\lambda_0$ [nm]	$\delta\lambda$ [nm]	spectral range
U	365	66	ultraviolet
B	445	94	blue
V	551	88	visual (green)
R	658	138	red
I	798	-	infrared

**Table 1.1:** The spectral setup of the Johnson filter system [2]

By measuring different filter constellations one can compute a distance-independent color index

$$m_B - m_V = M_B - M_V = B - V \quad (1.9)$$

which gives us information on the spectral properties of the object. Here  $m$  describes the apparent magnitudes and  $M$  the respective absolute magnitudes.

To correct any fractional deviations from a perfect filter system, the following correction formula, including the apparent magnitude  $B$  in the Johnson system and the measured instrumental magnitude  $b$ , is presented:

$$B = b + b_0 + c_B(b - v) + a_b \cdot \text{airmass} \quad (1.10)$$

The other correction terms have to be computed again by comparison with standard stars. The assumption made to obtain this formula was a slightly different transmission curve for the  $B$  filter.

## 1.6 The Hertzsprung-Russel Diagram

After having classified enough stars through observation, astronomers were able to perform statistical analysis.

It was noticed, that the spectral classification of stars is related to some basic parameters such as mass or luminosity. For example the so called  $O$  stars, which are located at the end of the classification scheme, were observed to be young, massive and luminous, whereas the  $M$  stars on the other side of the scheme have low mass and are barely visible.

This fundamental relation between the spectral type of a star, which is physically connected to its effective temperature  $T_{\text{eff}}$ , and its luminosity can be visualized in a *Hertzsprung-Russel diagram* (HRD).

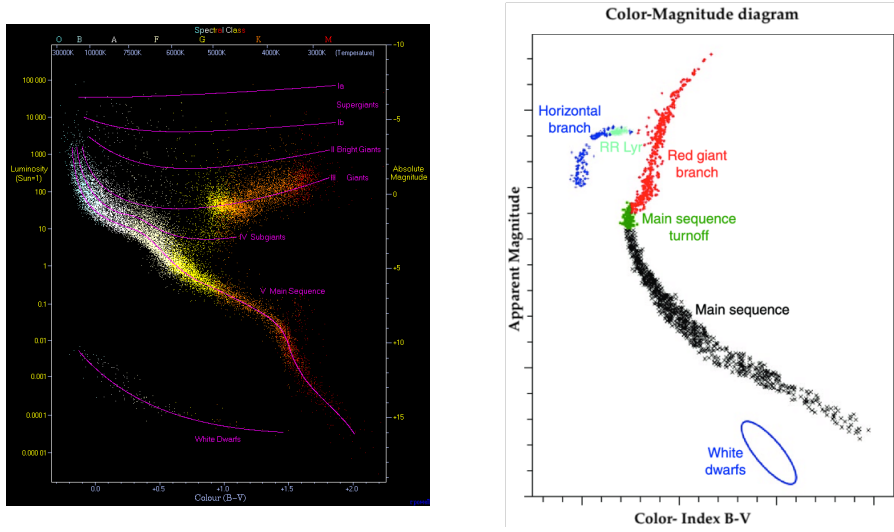


**Figure 1.2:** An observational HRD with 22.000 plotted stars from the Hipparcos catalogue<sup>4</sup> and a schematic picture of a CMD showing the most important domains.<sup>5</sup>

One can easily see, that most stars are located near the so called main sequence, which is characterized by the hydrogen burning phase during the main phase of a star's life. In the other regions of the diagram we can find stars in different stages of their life, e. g white dwarfs located below or giants above the main sequence.

As a conclusion one can remark that the HRD shows the evolutionary history of the population.

It's always hard to compute a HRD because, as already mentioned above, the absolute magnitudes or luminosities are often not accessible. The same is valid for the determination of the respective spectral classes.

Instead, astronomers use *Color-Magnitude diagrams* to visualize the evolution of star clusters. Here, the apparent magnitude  $V$  is plotted over the color index  $B - V$  which is related to  $T_{\text{eff}}$ . To obtain the color index, measurements with at least two filters are needed.

In the following we want to discuss how one can access the relevant data such as the distance, the age, or the metallicity of the population from the CMD.

## Analysis of a Color Magnitude Diagram

First of all we assume that all stars of a cluster are approximately equidistant to earth, have the same chemical composition and the same age.

By plotting  $V$  versus  $B - V$  and comparing the position of the main sequence of the cluster with a known cluster, the distance can be estimated. In this approximation we neglect small effects due to varying metallicities.

<sup>4</sup>Source: [https://en.wikipedia.org/wiki/Hertzsprung–Russell\\_diagram](https://en.wikipedia.org/wiki/Hertzsprung–Russell_diagram) (16.11.2018)

<sup>5</sup>Taken from: <https://www.researchgate.net/publication/10964320> (Slightly adapted, 18.11.2018)

The shift that is needed to align the main sequence with the one from the known cluster is proportional to the distance modulus of the cluster.

Alternatively one can always compare the CMD with theoretical models for stellar evolutions which are nowadays broadly known.

What we are doing in our evaluation of the cluster is applying a fitting routine to find the positions of the so called *isochrones*, e.g. the curves representing the position of the stars of the same age inside the population.

Another assumption, that all stars of the population were formed approximately at the same time, gives us the possibility to determine the age of the cluster from the CMD.

To understand how this is possible, one needs to know how the luminosity of stars is dependent on their mass:

$$L \sim M^a \quad (1.11)$$

The exponent  $a$  has a mass dependence itself (Here:  $a = 3.5$  for  $2M_{\odot} < M < 20M_{\odot}$ ).

One can conclude, that the massive stars on the top left end of the CMD drift to the red giant branch after all their hydrogen has been burned. The older stars with lower masses also start at some point to move into the red giant branch.

The time a star spends on the main sequence is proportional to the ratio  $\frac{M}{L}$ , e.g.

$$\tau_{\text{nuc}} \sim \frac{M}{L} = M^{(1-a)} \quad (1.12)$$

The shifting points in the sequence are called the *turn-off points*. From the position of the turn-off point one can estimate the age of the cluster. This method leads to good results, especially for older populations. In our fits later in the evaluation part we also vary the metallicity to obtain the best possible fit curve.

## 1.7 Stellar clusters

This section mainly deals with the classification and the comparison of the two main groups of stellar clusters: Open clusters and globular clusters (GC).

### 1.7.1 Open clusters

An open cluster is a group of up to a few thousand stars that have roughly the same age. More than 1000 open clusters have been discovered within the Milky Way and many more are thought to exist.

They are weakly bound by gravitational attraction and become disrupted by close encounters with other clusters and clouds of gas as they orbit the galactic center.

Their lifetime is estimated from a few hundred million years up to a few billion years for the most massive ones.

The metallicity of stars in an open cluster varies a lot, depending on age and location within the host galaxy. Normally they are distributed in the disc of the galaxy.

### 1.7.2 Globular clusters

In this experiment we are dealing with globular clusters, which are in general much older and more massive than the open clusters. They are among the oldest objects in the universe. Other characteristics are that the stars in a GC have a poor metallicity because they consist almost only of hydrogen and helium. This can be explained by the fact, that these were the elements found directly after the big bang. This indicates that the GC must have been formed in the early universe.

They are spherically symmetric and located in the halo of a galaxy. For the Milky Way, around 150 GCs are known. Because they were formed at the early phase of the galaxy's formation they are good references to study their evolution.

In general we can conclude that stellar clusters are well-suited for analysis with HRDs or CMDs because the respective diagrams have characteristic forms and therefore it is relatively easy to locate the stars within the diagrams.

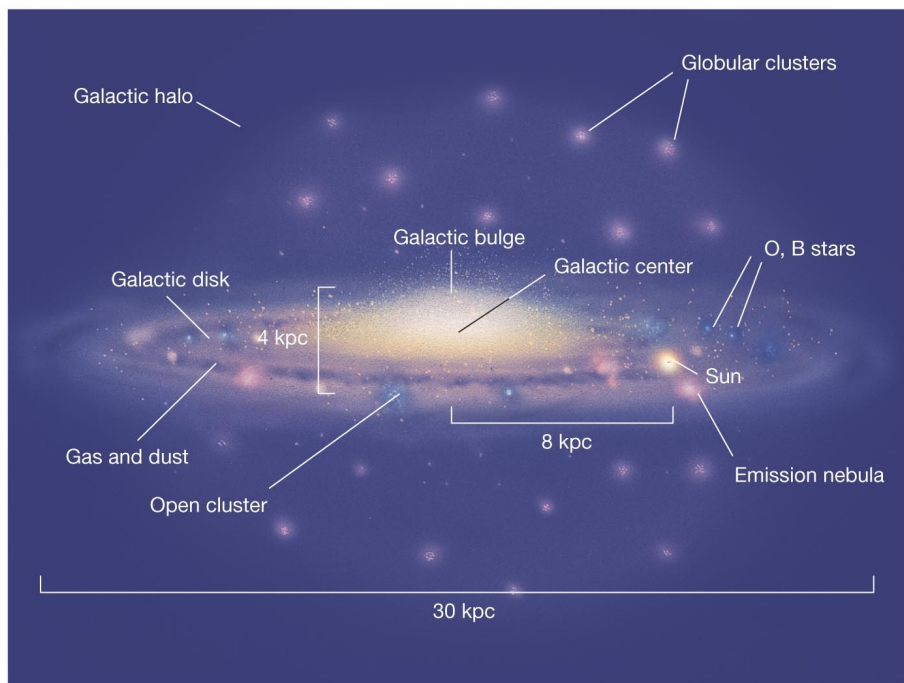


**Figure 1.3:** Illustration of the Milky Way with the characteristic positions of the different stellar clusters.<sup>6</sup>

<sup>6</sup>Source: <https://geopoliticraticus.files.wordpress.com/2011/08/milky-way-schematic.jpg> (18.11.18)

## 2 Layout of the experiment

The experiment is partly performed with the 70cm KING telescope at the Max-Planck-Institute for Astronomy on Königsstuhl. Its exact setup is depicted in figure (2.1).

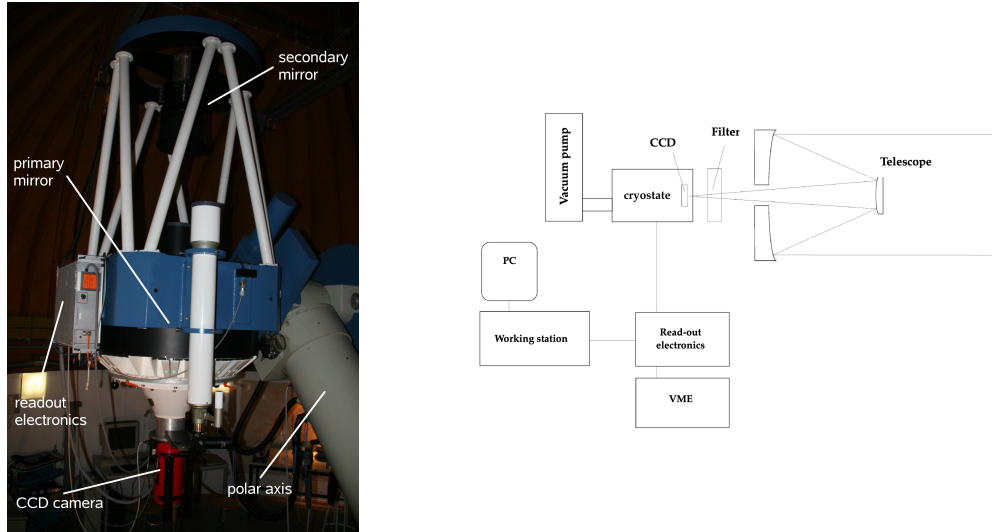


**Figure 2.1:** The KING telescope at MPIA and a schematic overview of our working station.  
Picture taken from [2] and slightly adapted.

The telescope has a parallactic mounting. After reflection by the primary mirror, with a diameter of 70 cm and the secondary mirror the light reaches the camera, which is cooled with liquid nitrogen and evacuated to about  $p = 10^{-6}$  mbar in order to minimize thermal conduction.

Our detector is a Loral/Lesser n2k2eb Bi thinned, back illuminated CCD, with a pixel scale of 0.55"/pixel. The pixels theoretically saturate at a level of 60000 electrons at a gain value of 5 which will be investigated later in the protocol.

In figure [2.1] on the right side, a schematic overview of our working station at MPIA is presented.

The data analysis part of this experiment was mostly performed on a local computer at MPIA. The software we used was IRAF, a well known system for this application with terrible user experience<sup>1</sup>. This is the reason why we switched to Python3, equipped with AstroPy, during the experiment.

The images were displayed with SAOImageDS9

<sup>1</sup>This obviously lies in the eye of the beholder.

# 3 Characteristics of the experimental setup

In this part we describe how we prepared the telescope and the detector system to be able to take images with a good quality and resolution.

More precisely, we are describing the cooling process, determining the band gap of our detector and we perform flat-field corrections. After that, we discuss further details of the properties of the CCD, which is located inside the detector.

## 3.1 The cooling process

Before we were able to start with our measurements, we had to prepare the telescope by cooling it down with liquid nitrogen to prevent disturbing effects such as thermal activation of electrons that could affect our measurements. First of all we evacuated the cryostat to protect the chip of damage caused by freeze out. This process took about three hours. Using a Python script, we took test images every thirty seconds to obtain the current temperature and to see the effects of the cooling process to the quality of the images. To demonstrate the impact on the resolution of the exposures we present two images, one taken at the beginning of the cooling process with a temperature of  $T_{\text{in}} = -4.7^{\circ}\text{C}$  and the other at the end, after reaching the final temperature  $T_{\text{f}} = -90.3^{\circ}\text{C}$ .

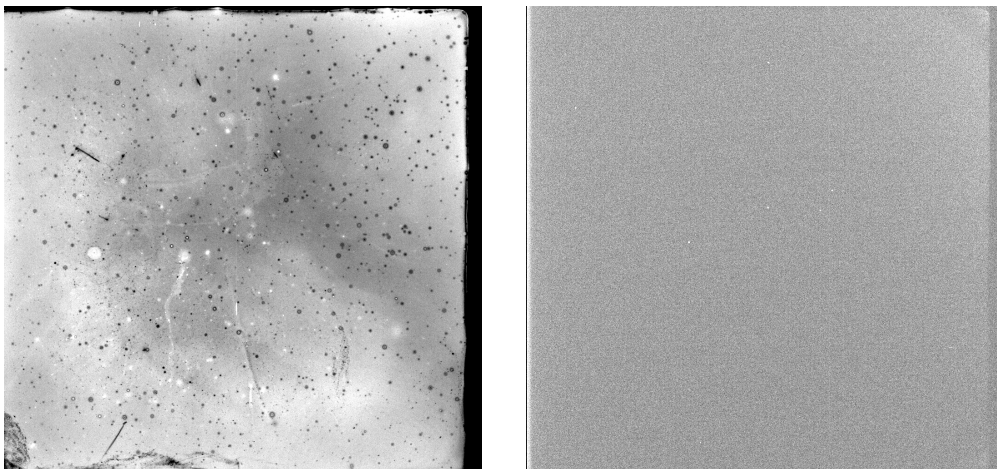


**Figure 3.1:** Visualization of the impact of the cooling process on the quality of the images.  
On the left one finds the picture taken at  $T = T_{\text{in}}$  on the right at  $T = T_{\text{f}}$ .

As one can easily see, the quality of the image improved a lot compared to the beginning of the measurement. The structure of the image is now almost homogeneous and we elim-

inated nearly all of the disturbing noise. In addition one can already see some of the dead pixels as small white parts which don't contribute to the measurement.

With the temperature data we were able to determine the band gap  $E_g$  of the semiconductor by fitting the theoretical curve which describes the dependency on the dark current  $I$  from the temperature  $T$  using Fermi statistics:

$$I = c_0 \cdot T^{\frac{3}{2}} \cdot \exp\left(-\frac{E_g}{2k_B T}\right) \quad (3.1)$$

The Boltzmann constant  $k_B$  is given by  $k_B = 8.617 \cdot 10^{-5} \text{ eV/K}$ . The result of our measurement is presented in the following diagram.

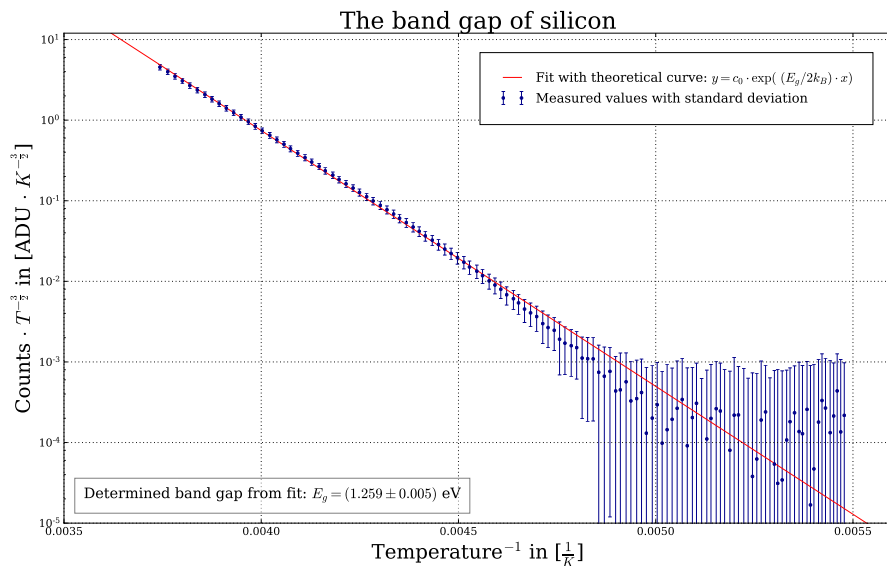


**Figure 3.2:** Determination of the band gap of silicon as an important characteristic of the experimental setup.

As a result of the measurement we determined the band gap for our detector:

$$E_g = (1.259 \pm 0.005) \text{ eV} \quad (3.2)$$

The theoretical value for silicon is  $E_{g,SI} = 1.15 \text{ eV}$  and therefore slightly smaller than the value we extracted from our temperature measurement.

For the value of the bias and its scatter we analyzed two pictures, one at the beginning and one at the end of the cooling process.

Temperature $T$ [°C]	bias [#counts]	scatter [#counts]
-4.7	1376	4
-90.3	1332	2

**Table 3.1:** Bias and its scatter.

## 3.2 Flat field corrections

To account for all variables in our setup we have to do flat field corrections for every filter (V-, I-, R-filter). For the calculation of a master flat field we took five images with relatively long integration time, that was determined experimentally before the measurements.

It is necessary to take multiple pictures for the master flat field, because some pixels are activated by cosmic background radiation. This is also the reason why we take the median of the values and not the mean. The mean will obviously be heavily influenced by a single far off value, while the median most likely remains almost the same.

The single images then were combined to the master flat field, which itself was normalized afterwards.

When correcting an image we divide it by the master flat field. This is the reason why normalization is important to actually be able to work with the master flat field because we only need relative and not absolute values.

To visualize the effect of the flat field corrections we performed one on an image we used to calculate the master flat field.

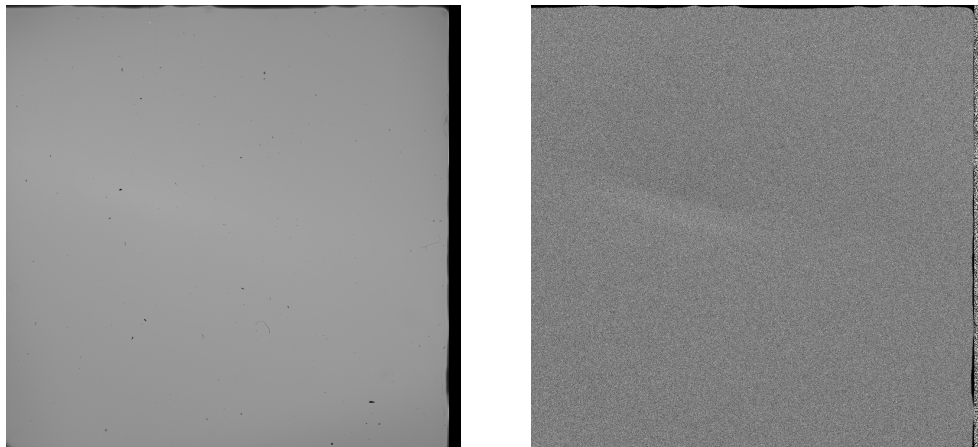


**Figure 3.3:** Impact of the master flat field correction on the quality of the image.  
The right picture shows the corrected version of the left picture.

Since the picture should only contain an illuminated surface we expect the corrected image to show a nearly homogeneous picture without any additional structures.

This is exactly what we see in figure [3.3], where the only visible differences in the corrected image are some errors, while the uncorrected image contains variations in intensity, tiny dust particles and other imperfections. The origin of these errors will be discussed later in the evaluation.

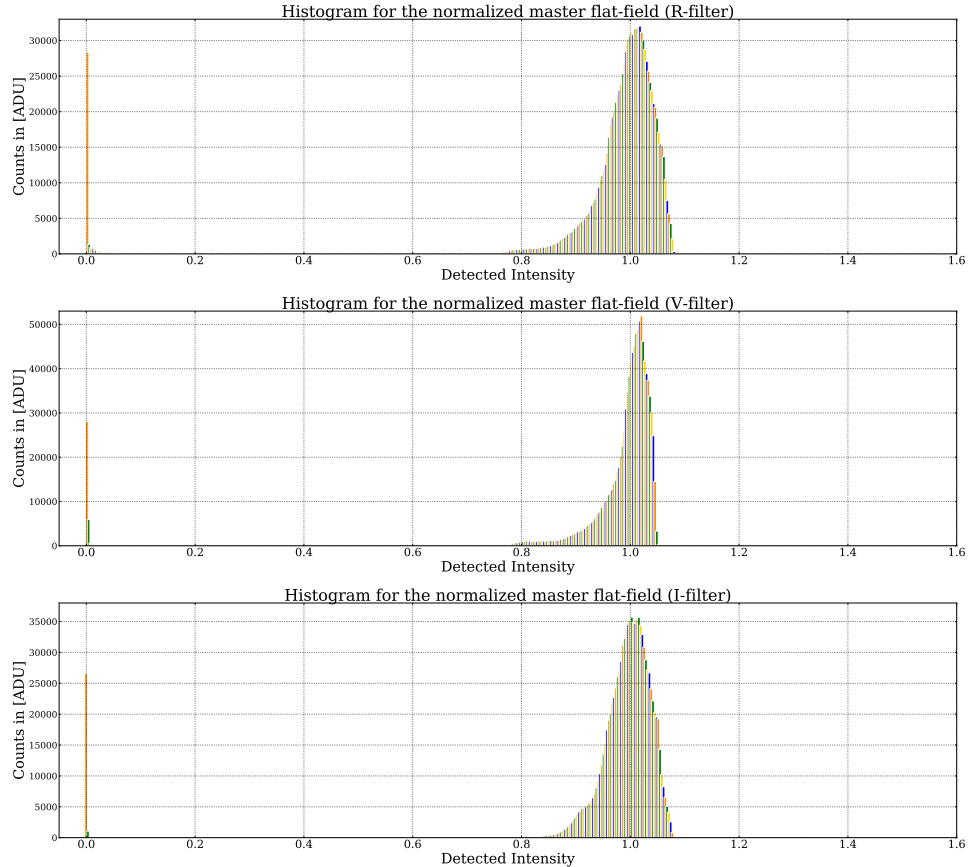


**Figure 3.4:** Histograms for the normalized intensity distributions for the three filter constellations.

The intensity variations and their distribution are best visible when they are plotted in a histogram, as was done for each filters master flat field in figure [3.4].

There is a noticeable peak at and very closely around zero on all the histograms, which is very likely caused by the dead pixels of the chip. The remaining distribution of counts describes the variations in the CCDs sensitivity, which highlights the importance of the master flat field correction, and is, as expected, centered around one. This can be explained by the fact that we chose the median count value as normalization factor.

When looking at the histograms, one also sees the slight variations in the distribution of the intensities for the different filter constellations. Every filter affects the optical path differently, also different wavelengths may have different quantum efficiencies. This means

it makes sense to obtain a separate master flat field for each filter.

The correction has to be done for every image taken with the CCD, because every image underlies these variations, and every image can be corrected this way.

### 3.3 Linearity and dynamical range of the CCD

This part of the experiment deals with the limitations of the chip concerning sensitivity to incoming photons, linearity and its dynamical range.

We measured with the same two different filter constellations as in the section before ( R- and I-filter).

By plotting the median of the signal against the adjusted integration time for both flat-field images we want to determine the linear regime of the electronics.

The result of the linear fit can be found in the following figure and is discussed after.

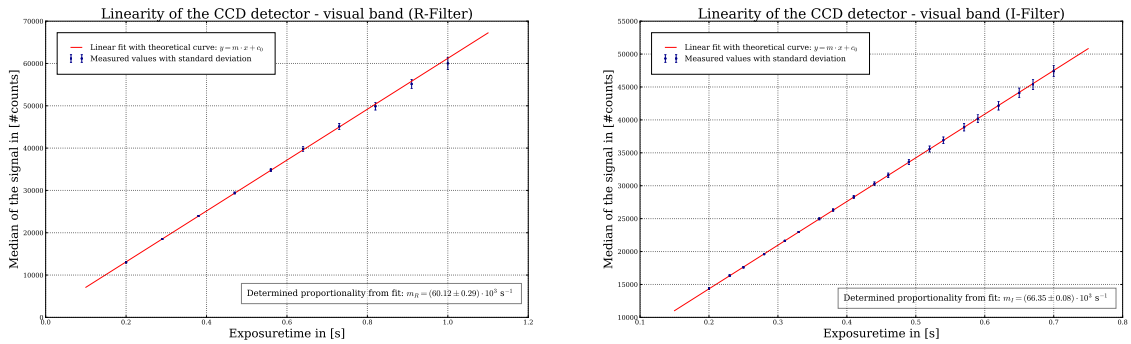


**Figure 3.5:** Results of the determination of the linear regime of the experimental setup with different filter constellations.

Unfortunately we didn't choose larger integration times to find the domain where the chip is saturated. Therefore we can only conclude which domains are definitely in the linear regime.

Nevertheless, we got the following results:

Filter	Counts <sub>min</sub>	Counts <sub>max</sub>	gain [counts/s]
R	~ 13000	~ 60000	(60.12 ± 0.29)
I	~ 14000	~ 48000	(66.35 ± 0.08)

**Table 3.2:** Determination of the linear regime of the measuring electronics for both filter constellations.

Now we want to investigate the deviation from a perfectly linear relationship by computing the  $R^2$  value for both fits. The  $R^2$  value is a statistical measure of how close the data

is to the fitted regression line. The formal definition is:

$$R^2 = \frac{\sum (\hat{y}_i - \bar{y})^2}{\sum (y_i - \bar{y})^2} = 1 - \frac{\sum (y_i - \hat{y}_i)^2}{\sum (y_i - \bar{y})^2} \quad (3.3)$$

where  $\hat{y}_i$  are the values predicted by the linear fit and  $\bar{y} = \frac{1}{n} \sum_i y_i$  is the mean of the measured values.

In our case we got the following results:

Filter	$R^2$ value
R	0.999567242841
I	0.999985446198

**Table 3.3:** Corresponding  $R^2$  values for our linear fits.

This means our results show a pretty much perfect linear relationship, as we expected.

### 3.4 Sensitivity of the detector and noise properties

For this part, the dark current was neglected, as described in the introduction. During the experiment, we used the I-filter and took 20 pairs of images with increasing integration time.

According to Poisson statistics, the error in each pixel scales with the number of incoming electrons  $N_e$  like

$$\sigma_e^2 = N_e \quad (3.4)$$

Together with the quantum efficiency  $\eta$  and gain  $\kappa$  of the CCD we have the following connection between incoming photons and measured electrons

$$N_e = \frac{\kappa}{\eta} N_{e,d} \quad (3.5)$$

$$\sigma_e^2 = \frac{\kappa^2}{\eta^2} \sigma_{e,d}^2 \quad (3.6)$$

The other noise sources are the read-out noise of the gate amplifier  $\sigma_R$  and the *Pixel Response Non-Uniformity* (PRNU) noise,  $\sigma_{PRNU}$ , that is caused by slight variations of the quantum efficiency in each pixel. The latter one should increase linearly with the incoming photons

$$\sigma_{PRNU,e} = N_e f_{PRNU} \quad (3.7)$$

with the detector dependent, characteristic factor  $f_{PRNU}$ . Therefore the total error is given by

$$\sigma_{\text{tot},d}^2 = \sigma_{e,d}^2 + \sigma_{R,d}^2 + \sigma_{PRNU,d}^2 \quad (3.8)$$

Since the PRNU is pixel dependent, we should get rid of it by subtracting two pixels with the same integration time from each other.

This leaves us with a total error of:

$$\sigma_{\text{diff},d}^2 = 2 (\sigma_{R,d}^2 + \sigma_{e,d}^2) \quad (3.9)$$

$$= 2 \left( \sigma_{R,d}^2 + \frac{N_{e,d}}{\kappa} \right) \quad (3.10)$$

We started with determining the total noise by calculating the standard deviation of a theoretically homogeneously illuminated area in one pair of images, which turned out to be  $\sigma_{\text{tot}} = (232.5 \pm 0.5)$ .

From the overscan region the read-out noise was determined to  $\sigma_{R,d} = 18.9$ .

With the formulae above this gives us a photon noise of  $\sigma_{e,d} = 47.3$  and a PRNU noise of  $\sigma_{PRNU,d} = 226.8$ .

Clearly the PRNU noise dominates the error. This is explained by equation (3.7) and the fact that we are dealing with intensities  $> 10000$ . Together with the estimate of order  $f_{PRNU} \sim 0.01$  this is what we expected.

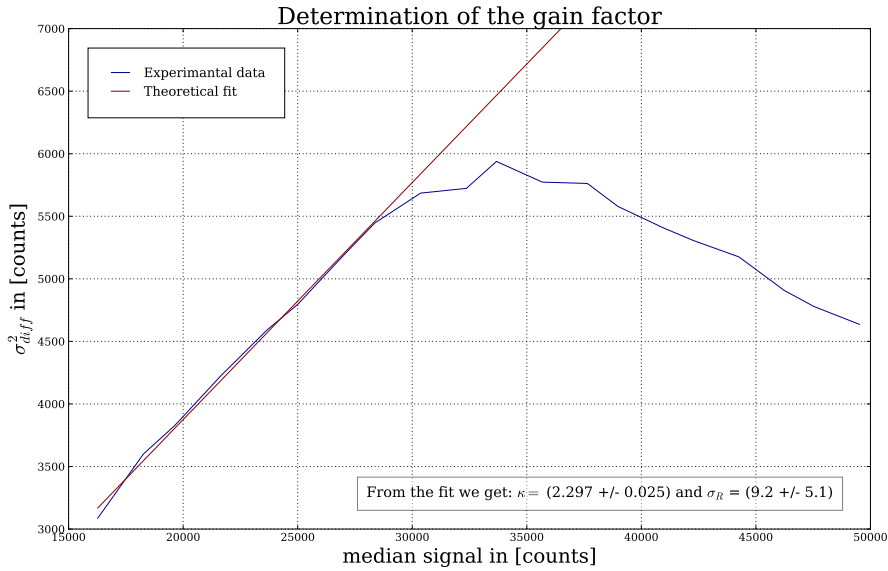


**Figure 3.6:** Determination of the gain factor of the CCD.

By fitting the linear part of our data, i. e. all the mean values up to 30000 counts, we were able to visualize equation (3.10) in figure [3.6].

This gives us a gain of  $\kappa = (2.297 \pm 0.025)$  and a read-out error of  $\sigma_R = (9.2 \pm 5.1)$ . The two values for our read-out error are therefore within the two sigma level.

At about 30000 mean counts some pixels already start to saturate, which causes the linear part to flatten out and eventually even decrease.

Another way to determine the gain is with

$$\sigma_{e,d}^2 = \frac{\eta}{\kappa} \quad (3.11)$$

which was derived from the formulae above. This leads to  $\kappa = 1.66$ , a value that is not within any error margin compared to the  $\kappa$  from our fit. But since the second  $\kappa$  was calculated by a standard deviation it was not possible to calculate its error, so the comparison is not entirely useful.

Another result of these calculations is that the read-out error is very small compared to the other errors. The quality of the analogue to digital converter (ADU) is therefore sufficient for our setup.

## 4 Globular Cluster BS90<sup>14</sup>

In this part of the experiment we are analyzing the properties of the globular cluster BS90<sup>14</sup>. Unfortunately the bad weather conditions during our measurement prevented us from collecting data ourselves. Instead we were working with images taken by the Hubble Space Telescope (HST).

The goal of this part is to perform PSF fitting for two different filter constellations, matching both images together and finally plot a Color Magnitude Diagram (CMD) to determine age and metallicity of the cluster after fitting different isochrones by varying both parameters.

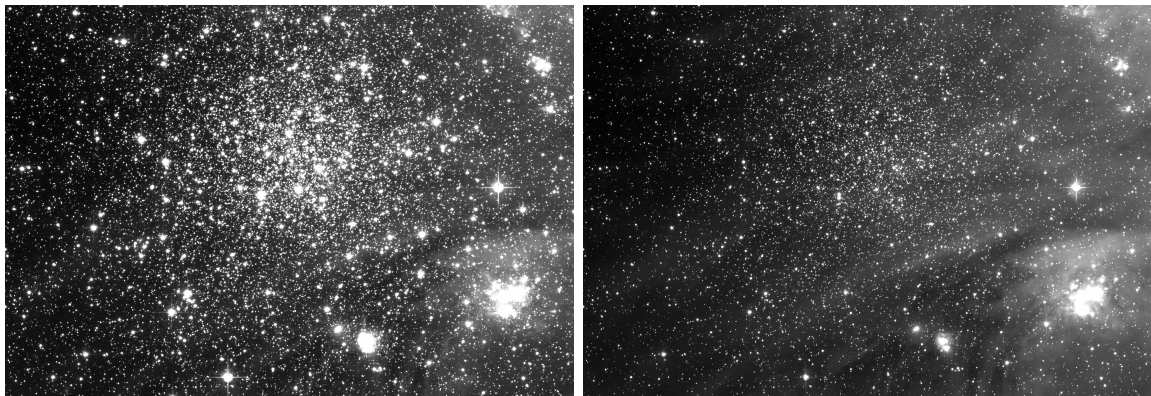


**Figure 4.1:** Exposures of the globular cluster BS90<sup>14</sup> taken by the Hubble Space Telescope. The image on the left was taken using an I-filter (infrared spectrum), the one on the right using a V-filter (visible spectrum).

### 4.1 Zeropoint calibration

To calibrate the measured data to a standard scale, which in this case is the apparent magnitude scale, we are comparing the counts of several standard stars with reference values from SIMBAD, an astronomical data base. From these results we can determine the zeropoint  $p_0$  using equation (1.4):

$$p_0 = m_{\text{CATALOG}} + 2.5 \log_{10}(\text{counts})$$

We chose ten suitable stars, i. e. stars that are clearly isolated and bright enough but not yet saturated.

The results of our measurement are enlisted in the following tables .

Star	Mag <sub>V</sub>	# <sub>V</sub>	$\Delta\#_V$	$p_{0,V}$	$\Delta p_{0,V}$	Mag <sub>I</sub>	# <sub>I</sub>	$\Delta\#_I$	$p_{0,I}$	$\Delta p_{0,I}$
1	17.78	908	30	25.175	0.036	16.65	1881	43	24.836	0.025
2	17.77	1371	37	25.613	0.029	16.21	4274	65	25.287	0.017
3	17.67	1345	37	25.492	0.030	16.81	3994	63	25.814	0.017
4	17.50	1052	32	25.055	0.033	16.64	2281	48	25.035	0.023
5	17.24	1511	39	25.188	0.028	15.79	4605	68	24.948	0.016
6	18.45	808	28	25.719	0.038	17.10	1738	42	25.200	0.026
7	18.23	885	30	25.597	0.037	16.23	2073	46	24.521	0.024
8	18.09	790	28	25.334	0.038	16.93	1626	40	24.958	0.027
9	17.97	961	31	25.427	0.035	16.68	1837	43	24.840	0.025
10	17.74	764	28	24.948	0.040	16.85	1694	41	24.922	0.026

**Table 4.1:** Zeropoint calibration by comparing ten stars with SIMBAD references. The left part corresponds to the exposure analyzed with the V-filter, the right part to the one analyzed with the I-filter.

**Remark:** Due to the limited space we abbreviated counts with #.

We take the mean of the calculated zeropoints  $p_0$  and compute the standard deviation as statistical error and the error propagation as usual to get an estimate of the systematic error.

The final results are the following:

Filter	zeropoint $p_0$	$\Delta p_0$ (syst.)	$\Delta p_0$ (stat.)
V	25.334	0.004	0.011
I	24.953	0.004	0.007

**Table 4.2:** Results of the zeropoint calibration.

## 4.2 PSF photometry with STARFINDER

We are using STARFINDER to perform statistical PSF fitting, e.g. the IDL takes the positions of about 10 to 30 isolated, unsaturated stars and applies several corrections (subtraction

of an average background and normalization of the peak intensities) to both images. Now the software is able to compare the results for all the stars we chose and to determine the final result: an average PSF for the entire image.

### The basic idea of PSF fitting

The point spread function (PSF) describes the response of an imaging system to point sources or point objects which are in our case the stars on the exposures. The degree of blurring of the point object is a measure for the quality of the image. An important characteristic is that the imaging of two different objects is independent of each other. This is due to the non-interacting property of photons. The image of a complex object can then be seen as a convolution of the true object and the PSF.

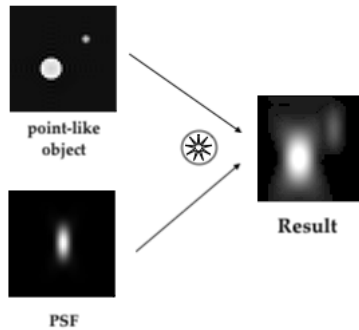


**Figure 4.2:** Visualization of the key idea of PSF fitting

The radiated field is related to its corresponding source plane distribution via Fourier transform. This is how the algorithm is able to determine the PSF from our exposures.

#### Applying this idea to our problem:

We chose about 25 stars and selected the most suitable, i. e. those who were as centered and symmetric as possible for the fitting.

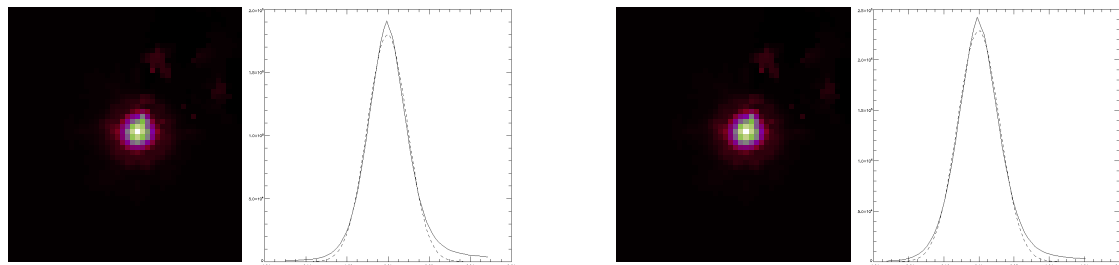


**Figure 4.3:** Results of the PSF fit for the I-filter (left) and the V-filter (right).

With these results, STARFINDER is able to detect all potential stars by dividing the image into smaller parts and checking if the analyzed objects are brighter than the estimated threshold. Using this technique, the program is only able to determine the instrumental magnitude of the sources. The result from the zeropoint calibration performed in (4.1) becomes important now, to get the corresponding apparent magnitudes. After finishing the iteration for both images, we get a list of all stars which could be detected.

To finally obtain the CMD for our cluster we need to match the stars found in both pictures. This cross matching process is done with the help of the Python script `matchstars.py` located on our working computer at MPIA.

### 4.3 Color Magnitude Diagram for BS90<sup>14</sup>

We are now able to plot the CMD (V versus V-I) and fit matching theoretical isochrones by varying different parameters in the script used for plotting (`cmdplot.py`, also available on the working computer) such as the shift of the image, the metallicity or the age of the cluster.

The resulting Color-Magnitude diagram is presented in figure (4.4):

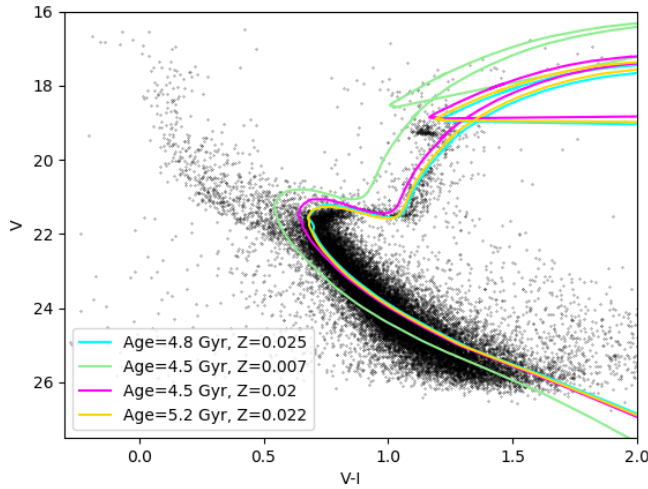


**Figure 4.4:** Color-Magnitude diagram with theoretical isochrones for BS90<sup>14</sup>

We fitted a total of four possible isochrones with different parameters. The quality of our results is discussed subsequently.

---

Isochrone [color]	Age [Gyr]	Metallicity $Z$
blue	4.8	0.025
green	4.5	0.007
magenta	4.5	0.020
yellow	5.2	0.022

**Table 4.3:** Fitting of the theoretical isochrones in our CMD.

The green isochrone doesn't seem to be a good reference, because one can clearly see that there is a large deviation between the curve and structure of the cluster.

We included it only due to the fact that the parameters chosen for this case match with the literature values.<sup>1</sup>

For all of the other curves we tried to find the best possible combination of parameters. Nevertheless we recognize a significant difference between the values for the metallicities we found and the value from the paper. Possible reasons for this deviation are discussed in the conclusion.

---

<sup>1</sup>Reference values can be found in this paper: <https://arxiv.org/pdf/0704.2942.pdf>

## 5 Discussion of our results

In this chapter we want to conclude our results and discuss possible reasons for deviations from what we would have expected.

**Characteristics of the CCD:** We determined the band gap of silicon by verifying the temperature dependency of the detected counts we expected from equation (3.1). Our result  $E_g = (1.259 \pm 0.005)$  eV is slightly higher the reference value for silicon (1.15 eV). This can have different reasons.

One possible explanation for the deviation is, that the result could be mainly affected by the measurements in the beginning of the cooling process, where we still had a lot of noise because of thermal activation. On top, the value for the band gap is not unique because it is still dependent on the temperature range we are observing. We worked on a large range of about 100 degrees. This means we have to take into account that the value for the band gap is not perfectly constant during all our measurements.

Another possible reason is that the silicon used in our measurement is not pure silicon or already shows some wear.

We repeated the temperature measurement every 30 seconds for the whole time of the cooling process. This should be enough to obtain sufficient precision and statistics.

We determined and subtracted an individual bias for every measurement to avoid an underestimation of the errors in the first part of the measurement and to present our results as general as possible.

We could have done more measurements in some specific temperature ranges to find out how much the band gap varies to confirm the problem we mentioned above.

**Flat field corrections:** We performed flat field corrections based on the determination of a normalized master flat field for every of the filter constellations.

As already discussed in the evaluation, it is quite useful to work in relative units when we want to have a good comparability of the results.

The impact of this correction method has impressively been shown by comparing the same exposure before and after dividing it by the master flat. The quality of the image improved a lot as one can see in figure (3.3).

The three histograms presented in figure (3.4) showed the expected distribution around the value 1 because this value represents the mean intensity which we normalized the images to. The effect of the dead pixels which do not contribute to the measurement is also clearly represented by the large peaks at zero.

---

**Linearity and Dynamical range:** In this part of the experiment we analyzed the linear domain of the measure electronics. Unfortunately we did not take enough measurements at higher integration times to find the expected plateau at the saturation level. Nevertheless we were still able to see the almost perfectly linear relationship for all our measured domain. This conclusion is supported by the calculation of the corresponding  $R^2$  values as explained before.

If we could repeat the measurement we would definitely take more values at high integration times to be really able to find the limitations of the electronics. At least we can conclude that our measurements shouldn't be affected too much by unwanted saturation.

**Sensitivity and noise properties:** In this part we learned how much our results are affected by the noise properties and the sensitivity of the experimental setup.

We found out that the PRNU noise dominates the other noises presented in this section. This is due the fact that we are working with high intensities.

The electron gain  $\kappa$  has been determined to:  $\kappa = (2.297 \pm 0.025)$  from the fit. This value was not directly comparable with the value we got from calculating  $\kappa$  by hand, using equation (3.11).

The read out noise  $\sigma_R = (9.2 \pm 5.1)$  is small compared to the other error sources. This leads us to the conclusion that the precision of the electronics is sufficient for our case.

**Globular Cluster BS90<sup>14</sup>:** In the final part of the experiment we worked on data concerning the globular cluster BS90<sup>14</sup>.

First we needed to find the zero point used for calibration of the magnitudes. Our determination was based on ten values for reference stars from the SIMBAD catalogue. To achieve a higher accuracy we could have taken more references into account. Our estimated errors are mainly based on statistical properties. Especially for this case one should take care of a large amount of reference values to find a useful estimate. The same holds for the next step, where we chose around 25 stars to be able to perform the PSF fitting. We repeated this selection three times to find the best possible result for STARFINDERs fitting routine.

After matching the stars found in both exposures we finally obtained the Color-Magnitude diagram which gave us the possibility to access the information about age and metallicity of the cluster.

The results presented in table (4.3) vary a lot compared to the reference value which is represented by the green isochrone. Especially the value for the metallicity is significantly different. It was nearly impossible to try out every possible combination of the parameters. That's the reason why we chose three different curves that matched quite good to be able to show how sensible these fitting routines are and how hard and ambiguous it is to find the *correct* values.

In general we can conclude that we learned a lot about astronomical research, especially about data analysis and image processing.

# List of Figures

1.1	Image of a CCD and a schematic overview of its functionality . . . . .	1
1.2	Hertzsprung-Russell diagram . . . . .	7
1.3	Illustration of the Milky Way . . . . .	9
2.1	The KING telescope at MPIA . . . . .	10
3.1	Impact of the cooling process . . . . .	11
3.2	Determination of the band gap of silicon . . . . .	12
3.3	Impact of the master flat field correction on the quality of the image . . . . .	13
3.4	Histograms for the normalized intensity distributions for the three filter constellations. . . . .	14
3.5	Determination of the linear regime . . . . .	15
3.6	Determination of the gain factor of the CCD. . . . .	17
4.1	Exposures of the globular cluster BS90 <sup>14</sup> . . . . .	19
4.2	Visualization of the key idea of PSF fitting . . . . .	21
4.3	Results of the PSF fit . . . . .	21
4.4	Color-Magnitude diagram with theoretical isochrones for BS90 <sup>14</sup> . . . . .	22

# References

- [1] Pierre Léna. *Observational Astrophysics*. 3. Auflage. Berlin ; Heidelberg: Springer, 2012.
- [2] Jörg-Uwe Pott. *FP 30: CCD photometry in modern astronomy - manuel*. Version 4.0.3. MPI for Astronomy, Heidelberg, 2017.
- [3] Albrecht Unsöld and Bodo Baschek. *Der neue Kosmos. Einführung in die Astronomie und Astrophysik*. 7. ed. Berlin ; Heidelberg: Springer Spektrum, 2015.

# Acknowledgements

We want to thank our supervisor Asmita for her constant support during the execution of the measurements and the help with the operation of IRAF, we had a lot of trouble with in the beginning.